IMECE2015-51939

IMPLEMENTATION AND VERIFICATION OF RKPM
IN THE SIERRA/SOLIDMECHANICS ANALYSIS CODE

David Littlewood[*]
Sandia National Laboratories
Albuquerque, NM
Email: djlittl@sandia.gov

Mike Hillman
University of California, San Diego
La Jolla, CA

Edouard Yreux
University of California, San Diego
La Jolla, CA

Joseph Bishop
Sandia National Laboratories
Albuquerque, NM

Frank Beckwith
University of California, San Diego
La Jolla, CA

Jiun-Shyan Chen
University of California, San Diego
La Jolla, CA

ABSTRACT

The reproducing kernel particle method (RKPM) is a mesh-free method for computational solid mechanics that can be tailored for an arbitrary order of completeness and smoothness. The primary advantage of RKPM relative to standard finite-element (FE) approaches is its capacity to model large deformations, material damage, and fracture. Additionally, the use of a meshfree approach offers great flexibility in the domain discretization process and reduces the complexity of mesh modifications such as adaptive refinement.

We present an overview of the RKPM implementation in the Sierra/SolidMechanics *analysis code, with a focus on verification, validation, and software engineering for massively parallel computation. Key details include the processing of meshfree discretizations within a FE code, RKPM solution approximation and domain integration, stress update and calculation of internal force, and contact modeling. The accuracy and performance of RKPM are evaluated using a set of benchmark problems. Solution verification, mesh convergence, and parallel scalability are demonstrated using a simulation of wave propagation along the length of a bar. Initial model validation is achieved through simulation of a Taylor bar impact test. The RKPM approach is shown to be a viable alternative to standard FE techniques that provides additional flexibility to the analyst community.*

INTRODUCTION

The modeling of large-deformation processes and material failure is an important and difficult problem in computational mechanics. Standard FE approaches often perform poorly in this regime due to mesh distortion, and may break down completely due to element inversion. Adaptive mesh refinement provides a means to maintain element quality, but entails significant computational complexity and expense. Simulations that include material separation in addition to large deformations require the capacity to model the evolution of discontinuities, for example via the extended finite element method (XFEM). The complexity and computational expense of these auxiliary techniques motivate the development of modeling approaches outside the framework of standard FE modeling.

RKPM is an alternative to mesh-based approaches that is well suited for problems involving large deformation and material failure [1, 2]. RKPM operates on a meshfree discretization and can be tailored for an arbitrary order of completeness and smoothness. Domain integration is achieved using one of several available formulations. Stabilized conforming nodal integration (SCNI) is the most accurate option for Lagrangian simulations [3, 4]. Alternatively, the stabilized non-conforming nodal integration (SNNI) formulation offers improved resilience under conditions of large deformation and material separation, but can suffer from convergence issues due to relaxation of the conform-

---

[*]Address all correspondence to this author.

ing conditions [5]. This shortcoming may be addressed using the variational consistency correction recently developed by Chen, Hillman, and Rüter [6], which restores optimal convergence. Additional stabilization can be provided for both SCNI and SNNI to suppress low-energy oscillatory modes that can manifest when the surface area to volume ratio is small [7].

RKPM has been recently implemented in the *Sierra/SolidMechanics* analysis code at Sandia National Laboratories [8]. To date, the implementation is restricted to explicit transient dynamics, with a focus on the efficient and robust solution of models with extensive contact subject to large, suddenly applied loads. The RKPM implementation interfaces directly with the *Sierra/SolidMechanics Library of Advanced Materials for Engineering* (LAME), which contains a broad set of constitutive models [9]. The meshfree discretization required for RKPM is created at the onset of a simulation through the conversion of a hexahedral or tetrahedral mesh. The mesh conversion process discards the initial element connectivity, but preserves node locations and the definitions of node sets for the application of initial and boundary conditions. Combined analyses employing both RKPM and standard FE approaches are enabled through application of the native *Sierra/SolidMechanics* contact algorithm.

An overview of the RKPM method, as implemented in *Sierra/SolidMechanics*, is presented below. The accuracy, convergence, and performance of the implementation are demonstrated though several test cases. Simulation of a propagating wave along the length of a bar provides an example of solution verification. A Taylor bar impact simulation demonstrates RKPM under large-deformation conditions and provides a means to evaluate the *Sierra/SolidMechanics* contact algorithm within a RKPM simulation.

METHODOLOGY

The RKPM formulation, and the corresponding software implementation, differ in several key ways from those of standard FE models. Notable differences include the requirements of the meshfree discretization, the need to communicate data over the RKPM support, which may cross processor boundaries, the absence of contact surfaces, and additional pre- and post-processing considerations (*e.g.*, visibility criteria defining permissible node interactions). Other aspects of RKPM, such as interaction with the time integrator and material model library, align well with the structure of FE software and do not necessitate significant code modification.

Solution Approximation

The RKPM approach operates on approximate solutions constructed over a meshfree discretization. This is in contrast to classical FE schemes in which the approximation space, and

the shape functions that define it, are tied directly to element connectivity.

Let the closed domain $\bar{\Omega} \subset \mathbb{R}^3$ be discretized by a set of NP nodes $\{\boldsymbol{x}_I | \boldsymbol{x}_I \in \bar{\Omega}\}_{I=1}^{NP}$. The nth order reproducing kernel (RK) approximation of a function $u(\boldsymbol{x})$ in $\bar{\Omega}$ denoted by $u^h(\boldsymbol{x})$ is:

$$u^h(\boldsymbol{x}) = \sum_{I=1}^{NP} \Psi_I(\boldsymbol{x}) u_I \tag{1}$$

where $\{\Psi_I(\boldsymbol{x})\}_{I=1}^{NP}$ is the set of RK shape functions and $\{u_I\}_{I=1}^{NP}$ is the set of coefficients of the approximation [1]. The shape functions are constructed by the product of a kernel function $\Phi_a(\boldsymbol{x} - \boldsymbol{x}_I)$ and a correction function $C(\boldsymbol{x}; \boldsymbol{x} - \boldsymbol{x}_I)$:

$$\Psi_I(\boldsymbol{x}) = \Phi_a(\boldsymbol{x} - \boldsymbol{x}_I) C(\boldsymbol{x}; \boldsymbol{x} - \boldsymbol{x}_I). \tag{2}$$

The kernel function has compact support $\Phi_I = \{\boldsymbol{x} \mid \Phi_a(\boldsymbol{x} - \boldsymbol{x}_I) \neq 0\}$ as shown in Figure 1, and the size of the support is denoted a. The kernel determines the smoothness of the approximation functions. A cubic B-spline function, for example, gives C^2 continuity. The correction function $C(\boldsymbol{x}; \boldsymbol{x} - \boldsymbol{x}_I)$ is composed of a linear combination of monomial basis functions in the following form:

$$C(\boldsymbol{x}; \boldsymbol{x} - \boldsymbol{x}_I) = \sum_{i+j+k=0}^{n} (x_1 - x_{I1})^i (x_2 - x_{I2})^j (x_3 - x_{I3})^k b_{ijk} \tag{3}$$

$$\equiv \boldsymbol{H}^T(\boldsymbol{x} - \boldsymbol{x}_I) \boldsymbol{b}(\boldsymbol{x}) \tag{4}$$

where $\boldsymbol{b}^T(\boldsymbol{x})$ is the row vector of the monomial coefficients $b_{ijk}(\boldsymbol{x})$ and $\boldsymbol{H}^T(\boldsymbol{x} - \boldsymbol{x}_I)$ is the row vector of the monomial bases:

$$\boldsymbol{H}^T(\boldsymbol{x} - \boldsymbol{x}_I) = \begin{bmatrix} 1 \ x_1 - x_{I1} \ \dots \ x_3 - x_{I3} \ (x_1 - x_{I1})^2 \ \dots \ (x_3 - x_{I3})^n \end{bmatrix}. \tag{5}$$

The coefficients $\boldsymbol{b}(\boldsymbol{x})$ are determined through the following reproducing conditions:

$$\sum_{I=1}^{NP} \Psi_I(\boldsymbol{x}) x_{I1}^i x_{I2}^j x_{I3}^k = x_1^i x_2^j x_3^k, \quad 0 \leq i + j + k \leq n. \tag{6}$$

With $\boldsymbol{b}(\boldsymbol{x})$ obtained from (6), the RK shape functions are constructed as

$$\Psi_I(\boldsymbol{x}) = \boldsymbol{H}^T(\boldsymbol{0}) \boldsymbol{M}^{-1}(\boldsymbol{x}) \boldsymbol{H}(\boldsymbol{x} - \boldsymbol{x}_I) \Phi_a(\boldsymbol{x} - \boldsymbol{x}_I), \tag{7}$$

$$\boldsymbol{M}(\boldsymbol{x}) = \sum_{I=1}^{NP} \boldsymbol{H}(\boldsymbol{x} - \boldsymbol{x}_I) \boldsymbol{H}^T(\boldsymbol{x} - \boldsymbol{x}_I) \Phi_a(\boldsymbol{x} - \boldsymbol{x}_I). \tag{8}$$
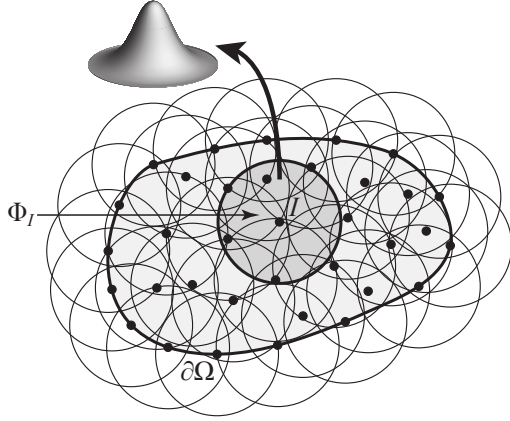
FIGURE 1. RKPM DOMAIN DISCRETIZATION WITH RK APPROXIMATION FUNCTIONS.

In the above, $\boldsymbol{M}(\boldsymbol{x})$ is termed the moment matrix. In this construction, the reproducing conditions (6) are met provided the moment matrix (8) is invertible, which requires sufficient non-coplanar points under the cover $\Phi_a(\boldsymbol{x} - \boldsymbol{x}_I)$ so that the reproducing equations are linearly independent [10].

By direct differentiation, the shape functions also satisfy the following important property for solving second order differential equations:

$$\sum_{I=1}^{NP} \nabla\Psi_I(\boldsymbol{x}) x_{I1}^i x_{I2}^j x_{I3}^k = \nabla(x_1^i x_2^j x_3^k), \quad 0 \le i+j+k \le n. \quad (9)$$

One important difference between RK shape functions and standard FE shape functions is that RK nodal coefficients are not the physical displacements at the nodes, *i.e.*, they lack the Kronecker delta property. Thus there is a distinction between the generalized displacements and the physical displacements at the nodes. To enforce boundary conditions in *Sierra/SolidMechanics*, boundary singular kernel functions are employed [11]. These modified RK shape functions restore the Kronecker delta property, allowing boundary conditions to be imposed directly.

Domain Integration

RKPM shape functions are rational, and can form complicated overlapping support structures that are difficult to integrate accurately. Because of this, the rate of convergence of the solution can be heavily influenced by the choice of domain integration method. Nodal integration presents an even greater challenge for meshfree methods since they suffer from both sub-optimal convergence and stability issues. The former is due to under-integration, while the latter is caused by severely under-estimating the energy for sawtooth modes. Advanced nodal in-
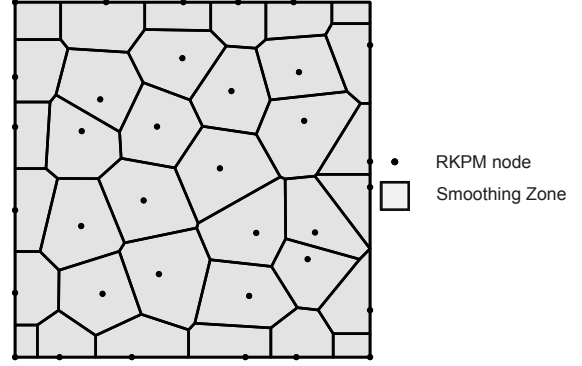
(a) Conforming smoothing zones for SCNI.
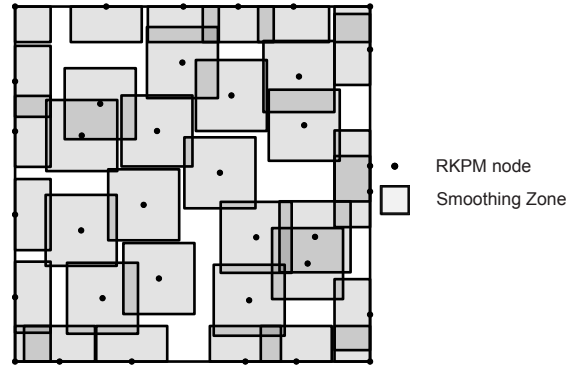
(b) Non-conforming smoothing zones for SNNI.

FIGURE 2. ILLUSTRATION OF RKPM SMOOTHING ZONES.

tegration methods which address these issues have been implemented in *Sierra/SolidMechanics*, as described below.

Stabilized conforming nodal integration (SCNI) was introduced in [3, 4] to remedy rank instability in direct nodal integration, and also to provide optimal convergence for linearly complete shape functions. In this method, gradients are smoothed over conforming nodal representative domains which partition the domain as shown in Figure 2(a), so that they are not evaluated directly at the nodes, thus avoiding rank instability.

The smoothing is also performed in such a way that the first order variational consistency condition for Galerkin linear exactness is satisfied, and optimal convergence is achieved. This condition requires satisfaction of the following divergence equality with the set of test functions and the chosen numerical integration [3, 6]:

$$\hat{\int_\Omega} \nabla\Psi_I(\boldsymbol{x})\, \mathrm{d}\Omega = \hat{\int_{\partial\Omega}} \Psi_I(\boldsymbol{x})\boldsymbol{n}(\boldsymbol{x})\, \mathrm{d}\Gamma \quad \forall I, \quad (10)$$

where "ˆ" denotes numerical integration, and $\Psi_I(\boldsymbol{x})$ is a shape function with first order completeness used in the Galerkin equation.

SCNI considers gradient smoothing with divergence in each nodal representative domain by

$$\tilde{\nabla}\Psi_I(\boldsymbol{x}_L) = \frac{1}{A_L}\int_{\Omega_L}\nabla\Psi_I(\boldsymbol{x})\,\mathrm{d}\Omega = \frac{1}{A_L}\int_{\partial\Omega_L}\Psi_I(\boldsymbol{x})\boldsymbol{n}(\boldsymbol{x})\,\mathrm{d}\Gamma. \quad (11)$$

Here $A_L = \int_{\Omega_L}\mathrm{d}\Omega$, Ω_L is the representative domain of node L, and Ψ_I are constants to be determined. The conforming nodal domains can be generated by, for example, Voronoi diagrams. In *Sierra/SolidMechanics*, a standard hexahedral or tetrahedral FE mesh is utilized to construct conforming cells at the initialization stage of an analysis.

The formation of conforming strain smoothing domains in SCNI can be cumbersome in problems subjected to topological change in geometry. To address this issue, stabilized non-conforming nodal integration (SNNI) [5,12] has been introduced as a simplification of SCNI. Figure 2(b) shows the gradient smoothing scheme by non-conforming cells constructed by considering box domains surrounding each node. The drawback of this simplification, however, is that (10) is no longer satisfied and SNNI does not always yield optimal convergence rates [6].

An assumed strain method can be utilized to achieve satisfaction of the first order variational consistency (VC) condition with SNNI. In this approach, an assumed gradient is introduced into the SNNI test functions [6]:

$$\hat{\nabla}\Psi_I(\boldsymbol{x}) = \tilde{\nabla}\Psi_I(\boldsymbol{x}) + R_I(\boldsymbol{x})\boldsymbol{\xi}_I, \quad (12)$$

where

$$R_I(\boldsymbol{x}) = \begin{cases} 1 & \text{if } \boldsymbol{x} \in \text{supp}(\Psi_I(\boldsymbol{x})) \\ 0 & \text{if } \boldsymbol{x} \notin \text{supp}(\Psi_I(\boldsymbol{x})) \end{cases}. \quad (13)$$

The form of the assumed gradient uncouples the VC equations, providing stability as well as computational efficiency. Substituting (12) into (10) with the assumed gradient, $\hat{\nabla}$, the coefficients are then solved for as

$$\boldsymbol{\xi}_I = \left(\int_{\partial\Omega}\hat{\Psi}_I(\boldsymbol{x})\boldsymbol{n}(\boldsymbol{x})\,\mathrm{d}\Gamma - \int_{\Omega}\tilde{\nabla}\Psi_I(\boldsymbol{x})\,\mathrm{d}\Omega\right)\left(\int_{\Omega}\hat{R}_I(\boldsymbol{x})\,\mathrm{d}\Omega\right)^{-1}. \quad (14)$$

Using this formulation, the test functions are variationally consistent with the SNNI integration scheme and optimal convergence associated with the linear completeness of the shape functions is achieved.

The energy of sawtooth modes may be underestimated in smoothed nodal integration methods as a result of insufficient
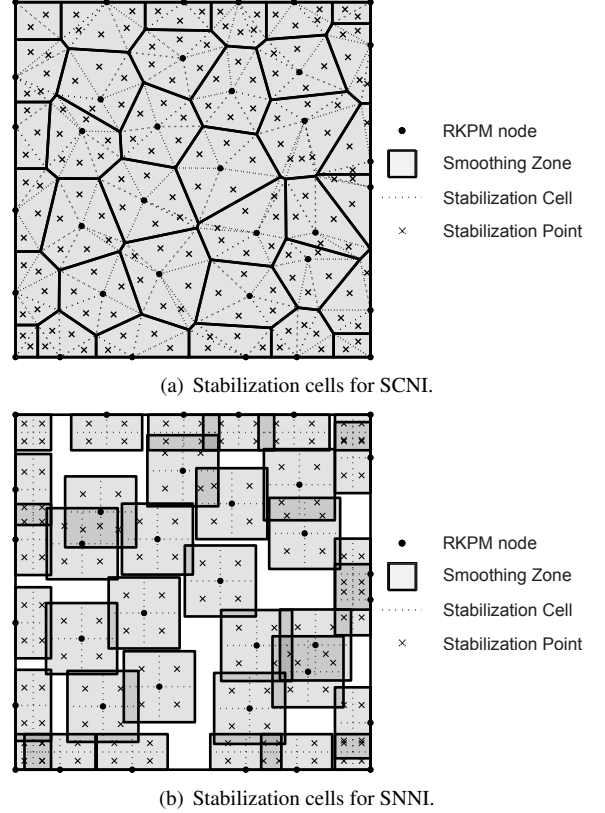

(a) Stabilization cells for SCNI.

(b) Stabilization cells for SNNI.

FIGURE 3. ILLUSTRATION OF RKPM STABILIZATION CELLS.

sampling when the surface area to volume ratio of the domain is small, or when the discretization is highly refined. Stabilization of these modes can be accomplished by introducing strain averaging over subdivisions of the smoothing cells to avoid the under-sampling of these modes [7]:

$$\begin{aligned}a(\boldsymbol{v}^h, \boldsymbol{u}^h)_{\text{stab}} &= \sum_{L=1}^{NP}\tilde{\boldsymbol{\varepsilon}}_L(\boldsymbol{v}^h) : \boldsymbol{C} : \tilde{\boldsymbol{\varepsilon}}_L(\boldsymbol{u}^h)V_L \\ &+ c\sum_{L=1}^{NP}\sum_{K=1}^{NS}(\tilde{\boldsymbol{\varepsilon}}_L(\boldsymbol{v}^h) - \boldsymbol{\varepsilon}_L^K(\boldsymbol{v}^h)) : \boldsymbol{C} : (\tilde{\boldsymbol{\varepsilon}}_L(\boldsymbol{u}^h) - \boldsymbol{\varepsilon}_L^K(\boldsymbol{u}^h))V_L^K,\end{aligned}$$
$$(15)$$

where $a(\boldsymbol{v}^h, \boldsymbol{u}^h)_{\text{stab}}$ is the modified bilinear form, NS is the number of stabilization points, $\tilde{\boldsymbol{\varepsilon}}_L$ is the smoothed strain at node L, $\boldsymbol{\varepsilon}_L^K$ is the strain at stabilization point K associated with node L, $\boldsymbol{C}$ is the matrix of material constants, c is a stabilization parameter ranging from zero to one, V_L is the cell volume associated with point L, and V_L^K is the sub-cell volume associated with point K. For SCNI, each nodal representative domain can be triangulated to form sub-cells as shown in Figure 3(a), and for SNNI, the smoothing zones can simply be partitioned into equal parts, as

4

shown in Figure 3(b).

The second term in (15) is the contribution of the stabilization; in explicit dynamics it leads to an additional internal force term. A key feature of this method is the fact that it does not upset variationally consistency in SCNI and VC-SNNI, and thus stabilized SCNI and VC-SNNI are convergent, stable, and also provide the efficiency of nodal integration.

Stress Update and Calculation of Internal Force

The RKPM approximation of the displacement field, described above, enables the calculation of kinematic quantities (*e.g.*, strains and strain rates) at each time step in the simulation. These kinematic quantities are passed to the constitutive model, which computes stresses. Nodal forces and the corresponding accelerations are then computed based on the stresses, allowing an explicit time integrator to advance the simulation to the subsequent time step. The *Sierra/SolidMechanics* implementation of RKPM interfaces directly with the *Library of Advanced Materials for Engineering*, providing access to a large number of constitutive models for computational solid mechanics [9].

Let $\boldsymbol{x}$ denote the current configuration of the body and $\boldsymbol{X}$ denote the reference configuration of the body. At any given time t^{n+1}, the main kinematic quantities of interest are the deformation gradient $\boldsymbol{F}$, and the symmetric part of the rate of deformation tensor $\boldsymbol{D}$,

$$F_{ij} = \frac{\partial x_i{}^{n+1}}{\partial X_j},$$
$$D_{ij} = \frac{1}{2\Delta t}\left(L_{ij} + L_{ji}\right), \tag{16}$$

where $\boldsymbol{L}$ is the spatial deformation gradient.

The deformation gradient $\boldsymbol{F}$ is computed by

$$F_{ij} = \sum_{J=1}^{NP} B_{Jj} u_{Ji}^{n+1} + \delta_{ij}, \tag{17}$$

where $B_{Ji} \equiv (\tilde{\nabla}\Psi_J)_i$ is the ith component of the smoothed material gradient of the shape function and $\boldsymbol{u}_J^{n+1}$ is the generalized nodal displacement at node J.

For the time step from t^n to t^{n+1}, $\boldsymbol{L}$ is computed in an incrementally objective manner by using the gradient with respect to the half time step configuration $\boldsymbol{x}^{n+1/2} = 1/2\left(\boldsymbol{x}^n + \boldsymbol{x}^{n+1}\right)$ [13],

$$L_{ij} = \frac{\partial \Delta u_i}{\partial x_j^{n+1/2}}, \tag{18}$$

where $\Delta \boldsymbol{u} = \boldsymbol{u}^{n+1} - \boldsymbol{u}^n$ is the increment of displacement. By applying the chain rule and employing smoothed gradient approximations, (18) is computed as

$$\boldsymbol{L} = \boldsymbol{D}\left(\boldsymbol{I} + \frac{1}{2}\boldsymbol{D}\right)^{-1}, \tag{19}$$

where $\boldsymbol{I}$ is the identity tensor and

$$D_{ij} = \sum_{J=1}^{NP} b_{Jj}\Delta u_{Ji}, \tag{20}$$

where $b_{Jj} = F_{jk}^{-1}B_{Jk}$ is the smoothed spatial gradient of the shape function and $\Delta\boldsymbol{u}_J$ is the generalized increment of nodal displacement at node J.

Due to the use of nodal integration, the above quantities are calculated at nodes rather than at Gauss points as in standard FE schemes. Cauchy stress at the current time step, $\boldsymbol{\sigma}^{n+1}$, is then computed through a call to the constitutive model based on the quantities in (16), and the internal force, $\boldsymbol{f}_{int}^{n+1}$, is determined using an updated Lagrangian formulation with nodal integration:

$$\boldsymbol{f}_{int}^{n+1} = \sum_{L=1}^{NP} \tilde{\boldsymbol{B}}^T(\boldsymbol{x}_L)\boldsymbol{\Xi}^{n+1}(\boldsymbol{x}_L)V_L, \tag{21}$$

where $\tilde{\boldsymbol{B}}^T(\boldsymbol{x}_L)$ and $\boldsymbol{\Xi}^{n+1}(\boldsymbol{x}_L)$ are Voigt notation vectors containing the smoothed spatial gradients b_{Ji} and stresses $\boldsymbol{\sigma}^{n+1}$, respectively, and V_L is the nodal volume in the current configuration. Nodal accelerations are computed directly from the nodal forces in (21), allowing the time integration routine to advance the simulation to the next time step.

An additional necessity for computational simulation using RKPM is estimation of the maximum stable time step. The critical time step for RKPM depends on the wave speed of the material, the type of domain integration, and the measure a of the kernel function $\Phi_a(\boldsymbol{x} - \boldsymbol{x}_I)$ selected in the approximation, which serves as the characteristic length for stability in time rather than nodal spacing as in standard FE approaches [14]. The time step is estimated based on these quantities at any given configuration in the simulation.

Creation of a Meshfree Discretization

Currently, the primary method for the construction of meshfree RKPM discretizations in *Sierra/SolidMechanics* is the direct conversion of hexahedral or tetrahedral meshes to a disconnected point cloud. This approach minimizes disruption of the standard analysis workflow. It allows for continued use of FE meshing software, and facilitates the straightforward conversion of previously-developed FE meshes to meshfree discretizations for RKPM. Under this approach, nodes present in the FE mesh,
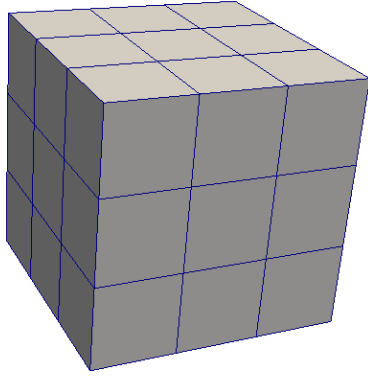
(a) Initial hexahedral mesh.
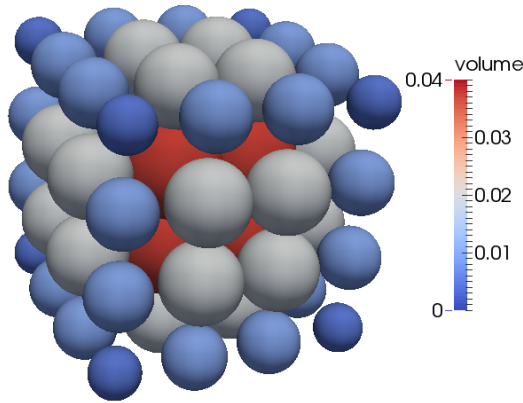
(b) Corresponding meshfree RKPM discretization.

FIGURE 4. CREATION OF A MESHFREE RKPM DISCRETIZA-
TION FROM A HEXAHEDRAL MESH OF A UNIT CUBE.

and the degrees of freedom associated with them, are left undisturbed. Element connectivity is deleted, and the mass associated with each of the original solid elements is distributed to one or more RKPM nodes. Further, to enable SCNI, conformal cells are defined for each RKPM node though a process in which the original elements are subdivided and the resulting sub-elements are grouped around the adjacent nodes. To date, *Sierra/SolidMechanics* supports the preservation of node sets defined on the original mesh for the application of prescribed displacement and velocity boundary conditions and initial conditions, but discards side set information (*i.e.*, sets of element faces). The application of pressure and traction boundary conditions to RKPM models is planned for future work.

The conversion process for a hexahedral mesh of a unit cube is illustrated in Figure 4. The hexahedral mesh, created using the *Cubit* [15] mesh-generation code, is shown in Figure 4(a), and the resulting meshfree discretization for RKPM is shown in Figure 4(b). Here, the size and color of the sphere glyphs illustrate the volume associated with each RKPM node.
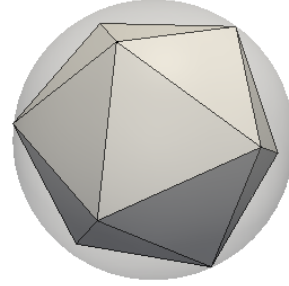
FIGURE 5. LOFTED CONTACT GEOMETRY FOR A RKPM
NODE.

Modeling Contact

The development of an effective contact modeling strategy for RKPM in *Sierra/SolidMechanics* is the subject of ongoing work. As part of the current study, the approach of utilizing lofted contact geometry was investigated as a means to enable the native *Sierra/SolidMechanics* contact algorithm for RKPM domains. The *Sierra/SolidMechanics* contact algorithm employs an iterative penalty approach to eliminate unphysical interpenetration and preserve linear momentum through a series of operations acting on planar facets [8, 16]. This approach is directly applicable to hexahedral and tetrahedral meshes, where planar faces are readily available from the element geometries, and skinning operations may be employed to identify domain boundaries. The use of the *Sierra/SolidMechanics* contact algorithm with RKPM requires the construction of a set of planar faces to define the contact surfaces. For this purpose, an icosahedron may be associated with each RKPM node in the contact domain. An illustration of the icosahedron contact geometry is given in Figure 5. The dimensions of the icosahedron may be provided by the analyst, or may determined automatically based on the nodal volume. In the second case, the icosahedron is constructed such that it is enclosed by the sphere centered at the node with a volume equal to the nodal volume. The enclosing sphere is illustrated as a gray circle in Figure 5.

While the use of lofted icosahedron geometry to enable contact for RKPM produces satisfactory results in many cases, several drawbacks exist. The foremost shortcoming is the lack of a contiguous contact surface. The smooth, water-tight surfaces associated with hexahedral and tetrahedral domains provide an efficient and reliable set of planar facets for evaluation of the contact algorithm. In contrast, the lofted icosahedra associated with a RKPM domain are not smooth, and may include gaps, particularly under large deformation. Further, the number of contact facets can grow large for RKPM domains, requiring additional computational expense.

An alternative approach, currently under consideration, makes use of the initial hexahedral or tetrahedral mesh, if available, for the definition of contact facets for a RKPM domain (see

Figure 4(a)). In this case, a skinning operation applied to the initial solid-element mesh identifies a set of faces that are preserved throughout the mesh-conversion process. These faces are then used as contact surfaces for the RKPM domain, eliminating the need for lofted geometry. It is anticipated that this approach will work well in the absence of material separation, but will present difficulties if the contact surfaces require updating, for example as a result of material failure.

BENCHMARK SIMULATIONS

Verification and validation (V&V) of the RKPM implementation requires extensive testing. A comprehensive V&V test suite includes solution verification, convergence studies, scaling studies, and validation of simulation results against experimental data. The example simulations presented below demonstrate the *Sierra/SolidMechanics* RKPM implementation and serve as initial test cases toward the goal of rigorous V&V.

Wave Propagation in a Bar

Propagation of a wave along a long, thin bar provides one instance of a solution verification test. A model of a bar was constructed with dimensions of 20.0 mm by 0.2 mm by 0.2 mm. The bar was modeled as elastic with a density of 7.8 g/cm^3. A one-dimensional solution was emulated by assigning a Young's modulus of 3.0e5 MPa and a Poisson's ratio of zero. The RKPM formulation employed a first order basis, a quartic B-spline kernel, SCNI domain integration, and a normalized support size of 1.6. The bar was given an initial velocity of 10.0 m/s, and a fixed displacement boundary condition was applied to the leading edge of the bar to simulate contact with a rigid body.

Results for the wave propagation simulation were verified against the following analytical solution,

$$u(x,t) = \sum_{n=1}^{\infty} \left(A_n \sin\left(\omega_n t\right) \sin\left(\frac{(2n-1)\pi}{2L} x \right) \right), \quad (22)$$
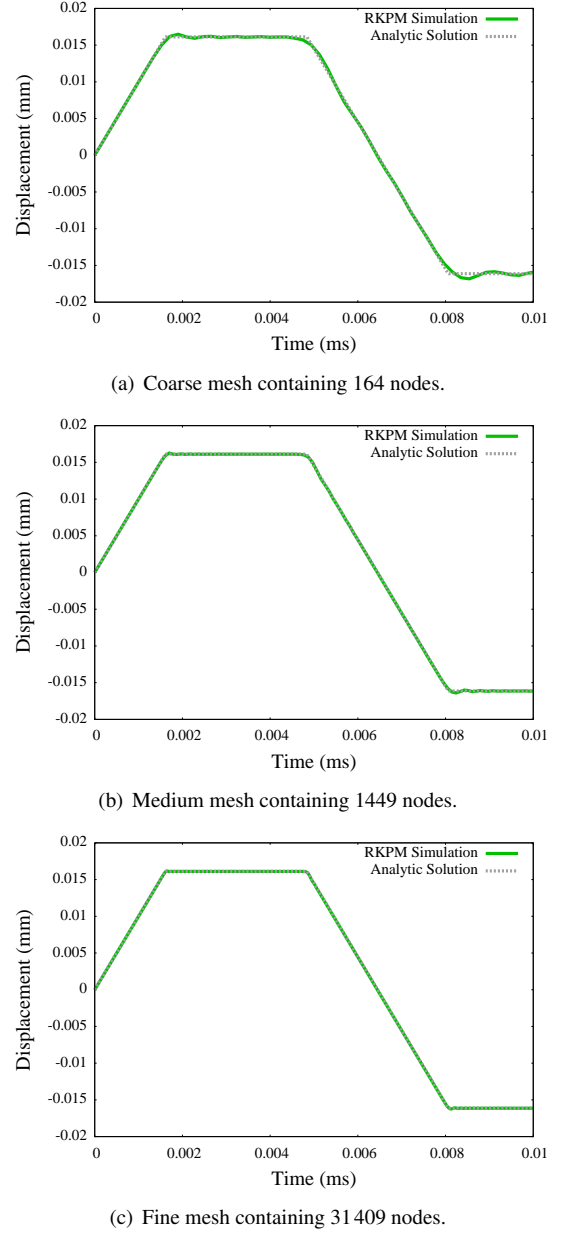
where

$$A_n = \frac{8 v_0 L}{(2n-1)^2 \pi^2} \sqrt{\frac{\rho}{E}}, \quad (23)$$

and

$$\omega_n = \frac{(2n-1)\pi}{2L} \sqrt{\frac{E}{\rho}}. \quad (24)$$

Here, $u(x,t)$ is the displacement at position x at time t, L is the length of the bar, v_0 is the initial velocity, ρ is the density of

(a) Coarse mesh containing 164 nodes.

(b) Medium mesh containing 1449 nodes.

(c) Fine mesh containing 31 409 nodes.

FIGURE 6. VERIFICATION OF DISPLACEMENT AT THE MID-POINT OF THE BAR IN THE WAVE PROPAGATION SIMULATION.

the bar, and E is the modulus. Agreement of the computational simulation and the analytical solution for several levels of mesh refinement are illustrated in Figure 6.

Parallel efficiency of the RKPM implementation was evaluated for the wave propagation simulation. A simulation utilizing a highly-refined discretization containing 360 192 nodes was carried out using 1, 2, 4, 8, 16, 32, 64, and 128 processors. The results of the scaling study, presented in Figure 7, demonstrate the effectiveness of the parallel implementation.
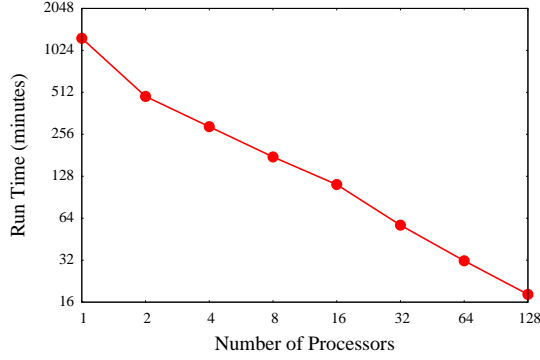
FIGURE 7. SCALING STUDY RESULTS FOR THE WAVE PROPAGATION SIMULATION.

Taylor Bar Impact Simulation

Simulations of a Taylor bar impact test [17–19] were carried out to evaluate the effectiveness of the RKPM implementation under large-deformation conditions. Following the experiments of Johnson and Cook [18, 19], a 4340-steel cylindrical bar with initial height $L_0 = 12.7$ mm and initial diameter $D_0 = 7.62$ mm was assigned a velocity of $v_0 = 282.0$ m/s prior to impacting a rigid target. The bar was modeled using RKPM with a first order basis, a quartic B-spline kernel, SNNI domain integration, and a normalized support size of 2.1. Initial simulations utilized a fixed-displacement boundary condition to model contact with the rigid target. Constitutive response was modeled using the Johnson-Cook material model [18, 19], in which a yield stress is defined as

$$\sigma_{eq} = \left(A + B\bar{\varepsilon}^n\right)\left(1 + \dot{\varepsilon}^*\right)^C \left(1 - T^{*m}\right), \qquad (25)$$

where $\bar{\varepsilon}$ is the equivalent plastic strain, and $\dot{\varepsilon}^* = \dot{\bar{\varepsilon}}/\dot{\varepsilon}_0$ represents the plastic strain rate normalized by a reference strain rate at which experiments were conducted to characterize the material. The normalized temperature $T^* = (T - T_0)/(T_m - T_0)$ is utilized to characterize thermal softening caused by adiabatic heating. The constitutive model parameters, taken from [19], are presented in Table 1.

Results for the Taylor bar simulation are presented in Figure 8. Large plastic strains were predicted at the leading edge of the bar as a result of material spreading at the impact surface. The RKPM model remained coherent in the large-deformation regime and was free from numerical difficulties. As expected, the fixed displacement boundary condition resulted in unbroken contact between the leading edge of the bar and the (fictitious) contact surface.

Simulation results for the final height of the specimen were validated against the experimental results of Johnson and Cook [18], in which the height of the bar after impact was mea-

TABLE 1. JOHNSON-COOK MATERIAL MODEL PARAMETERS FOR THE TAYLOR BAR SIMULATION [19].

Parameter	Value
Young's modulus E	200 GPa
Poisson's ratio ν	0.29
Density ρ	7830 kg/m^3
Specific heat capacity C_p	477 J/kgK
Initial temperature T_0	300 K
Melting temperature T_m	1793 K
Temperature softening exponent m	1.03
Yield stress A	792 MPa
Strain hardening coefficient B	510 MPa
Strain hardening exponent n	0.26
Strain rate hardening exponent C	0.014
Reference strain rate $\dot{\varepsilon}_0$	1.0 s^{-1}
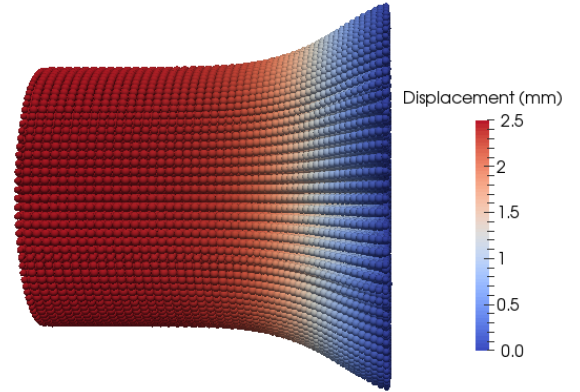
FIGURE 8. TAYLOR BAR IMPACT SIMULATION WITH FIXED DISPLACEMENT BOUNDARY CONDITION. COLOR DENOTES DISPLACEMENT IN THE HORIZONTAL DIRECTION.

sures as $L_f = 0.812L_0$. Results for simulations using different levels of mesh refinement are presented in Figure 9. The coarse, medium, and fine discretizations contained 938, 26 488, and 46 592 nodes, respectively. Results for the medium and fine discretizations are nearly identical, indicating mesh convergence, and are in good agreement with the experimental data. The oscillations in the final height of the bar are a result of the elastic response of the constitutive model and are expected in the absence of damping.
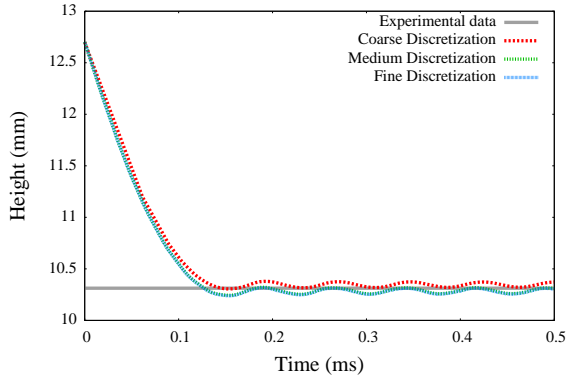
FIGURE 9.   COMPUTED FINAL HEIGHT OF TAYLOR BAR.

FIGURE 10. TAYLOR BAR IMPACT SIMULATION WITH CONTACT. COLOR DENOTES DISPLACEMENT IN THE HORIZONTAL DIRECTION.

Modeling Contact within the Taylor Bar Simulation

Additional simulations of the Taylor bar impact experiment were carried out to evaluate the effectiveness of the native *Sierra/SolidMechanics* contact algorithm for modeling contact between a RKPM domain and a domain modeled with standard hexahedral elements. As discussed above, the contact algorithm operates on surfaces comprised of planar facets. Contact facets for the RKPM domain were created using the lofted icosahedron approach illustrated in Figure 5.

Results from a Taylor bar simulation with contact are presented in Figure 10. The discretization shown in Figure 10 is identical to that of Figure 8, the only exception being the use of a deformable target modeled with standard hexahedral elements. In contrast to the simulation utilizing a fixed displacement boundary condition, the bar in the contact simulation separates from the impact surface at the outer radius of the leading end of the bar. In addition, the inclusion of a deformable target allows for the transfer of energy from the bar to the target, and the subsequent propagation of waves through the target material.

DISCUSSION AND CONCLUSIONS

RKPM was implemented in the *Sierra/SolidMechanics* analysis code with the goal of providing an enhanced simulation capability in the regime of large deformation and material failure. The implementation is restricted to explicit transient dynamics and currently employs the native *Sierra/SolidMechanics* contact algorithm, which facilitates interaction between RKPM domains and standard FE domains. Functionality was implemented for the conversion of hexahedral and tetrahedral meshes to meshfree discretizations for RKPM, including the creation of conformal cells for SCNI. Preliminary V&V efforts have verified RKPM against the analytical solution for wave propagation along a bar, and validated RKPM as a means to capture large-deformation material response though simulation of a Taylor bar impact test.
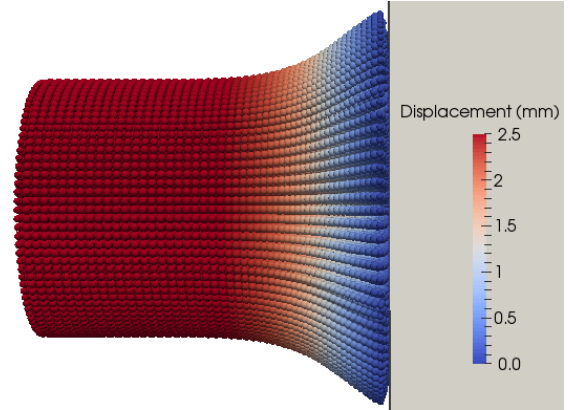
Ongoing Work

The implementation and testing of RKPM in *Sierra/SolidMechanics* completed to date provides the groundwork for several ongoing efforts.

The first is implementation of a semi-Lagrangian RKPM formulation that is applicable to problems involving material failure [5,12]. The future development of a semi-Lagrangian formulation is the primary motivation for the inclusion of SNNI functionality in the current implementation. Unlike the Lagrangian scheme, the proximity search that establishes nodal interactions is repeatedly updated under the semi-Lagrangian approach to reflect the deformed configuration. The updating of nodal interactions is a necessity for capturing material behavior under conditions of pervasive damage.

Improved contact algorithms for RKPM are also under consideration for inclusion in *Sierra/SolidMechanics*. Utilizing the interaction of meshfree kernel functions, contact algorithms can be implemented which naturally satisfy the impenetration condition [20]. In this approach, the pairwise interactions of nodes due to overlapping kernels induce stresses. The stick and slip conditions are then calculated based on the tangential stress using Coulomb's contact friction law. Using level set representations of the boundaries of the two bodies, surface normals necessary for this calculation are obtained using only nodal data.

An additional topic of ongoing research is the direct creation of meshfree discretizations from domain geometry data. The approach advocated above, in which a pre-existing hexahedral or tetrahedral mesh is converted to a meshfree discretization, does not take full advantage of the flexibility of meshfree models. The direct creation of a meshfree discretization from domain geometry data offers promise for rapid design-to-analysis applications, and for the the optimization of the discretization process for any number of user-defined objectives.

REFERENCES

[1] Liu, W. K., Jun, S., and Zhang, Y. F., 1995. "Reproducing kernel particle methods". *International Journal for Numerical Methods in Fluids,* **20**, pp. 1081–1106.

[2] Chen, J.-S., Pan, C., Wu, C.-T., and Liu, W. K., 1996. "Reproducing kernel particle methods for large deformation analysis of non-linear structures". *Computer Methods in Applied Mechanics and Engineering,* **139**, pp. 195–227.

[3] Chen, J.-S., Wu, C.-T., Yoon, S., and You, Y., 2001. "A stabilized conforming nodal integration for galerkin mesh-free methods". *International Journal for Numerical Methods in Engineering,* **50**, pp. 435–466.

[4] Chen, J.-S., Yoon, S., and Wu, C.-T., 2002. "Non-linear version of stabilized conforming nodal integration for galerkin mesh-free methods". *International Journal for Numerical Methods in Engineering,* **53**, pp. 2587–2615.

[5] Guan, P. C., Chi, S. W., Chen, J.-S., Slawson, T. R., and Roth, M. J., 2011. "Semi-lagrangian reproducing kernel particle method for fragment-impact problems". *International Journal of Impact Engineering,* **38**, pp. 1033–1047.

[6] Chen, J.-S., Hillman, M., and Rüter, M., 2013. "An arbitrary order variationally consistent integration for galerkin meshfree methods". *International Journal for Numerial Methods in Engineering,* **95**, pp. 387–418.

[7] Puso, M. A., Chen, J.-S., Zywicz, E., and Elmer, W., 2008. "Meshfree and finite element nodal integration methods". *International Journal for Numerical Methods in Engineering,* **74**, pp. 416–446.

[8] SIERRA Solid Mechanics Team, 2015. Sierra/SolidMechanics 4.36 user's guide. SAND Report 2015-2199, Sandia National Laboratories, Albuquerque, NM and Livermore, CA.

[9] Scherzinger, W. M., and Hammerand, D. C., 2007. Constitutive models in LAME. SAND Report 2007-5873, Sandia National Laboratories, Albuquerque, NM and Livermore, CA.

[10] Han, W., and Meng, X., 2001. "Error analysis of the reproducing kernel particle method". *Computer Methods in Applied Mechanics and Engineering,* **190**, pp. 6157–6181.

[11] Chen, J.-S., and Wang, H.-P., 2000. "New boundary condition treatments in meshfree computation of contact problems". *Computer Methods in Applied Mechanics and Engineering,* **187**, pp. 441–468.

[12] Guan, P. C., Chen, J.-S., Wu, Y., Teng, H., Gaidos, J., Hofstetter, K., and Alsaleh, M., 2009. "Semi-lagrangian reproducing kernel formulation and application to modeling earth moving operations". *Mechanics of Materials,* **41**, pp. 670–683.

[13] Hughes, T. J. R., and Winget, J., 1980. "Finite rotation effects in numerical integration of rate constitutive equations arising in large-deformation analysis". *International Journal for Numerical Methods in Engineering,* **15**, pp. 1862–1867.

[14] Belytschko, T., Guo, Y., Liu, W. K., and Xiao, S. P., 2000. "A unified stability analysis of meshless particle methods". *International Journal for Numerical Methods in Engineering,* **48**, pp. 1359–1400.

[15] *Cubit* mesh generation code. http://cubit.sandia.gov.

[16] Brown, K. H., Glass, M. W., Gullerud, A. S., Heinstein, M. W., Jones, R. E., and Voth, T. E., 2004. ACME: Algorithms for contact in a multiplysics environment, API version 2.2. SAND Report 2004-5486, Sandia National Laboratories, Albuquerque, NM and Livermore, CA.

[17] Wilkins, M. L., and Guinan, M. W., 1973. "Impact of cylinders on a rigid boundary". *Journal of Applied Physics,* **44**, pp. 1200–1206.

[18] Johnson, G. R., and Cook, W. H., 1983. "A constitutive model and data for metals subjected to large strains, high strain rates and high temperatures". In Proceedings of the 7th International Symposium on Ballistics, pp. 541–547.

[19] Johnson, G. R., and Cook, W. H., 1985. "Fracture characteristics of three metals subjected to various strains, strain rates, temperatures and pressures". *Engineering Fracture Mechanics,* **21**, pp. 31–48.

[20] Chi, S.-W., Lee, C.-H., Chen, J.-S., and Guan, P.-C., 2015. "A level set enhanced natural kernel contact algorithm for impact and penetration modeling". *International Journal for Numerial Methods in Engineering,* **102**, pp. 839–866.